On the Use of an Electro-Mechanical and a Solid-State Switching Matrix for a Portable Microwave-based Brain Stroke Scanner

On the Use of an Electro-Mechanical and a Solid-State Switching Matrix for a Portable Microwave-based Brain Stroke Scanner

M. Gugliermino, *Student Member, IEEE*, D. O. Rodriguez-Duarte, *Member, IEEE*, C. Origlia, *Student Member, IEEE*, J. A. Tobon Vasquez, *Member, IEEE*, R. Scapaticci, *Member, IEEE*, J. Ch. Bolomey, *Life Fellow Member, IEEE*, L. Crocco, *Senior Member, IEEE* and F. Vipiana, *Senior Member, IEEE*

***Abstract*—This paper examines the effects of the switching matrix on a multi-view and low-complexity portable microwave imaging system for brain stroke monitoring. It considers two switching solutions: an ad-hoc one relying on RF electromechanical switches and a compact off-the-shelf one using solid-state switches. The performed analysis deems path attenuation and inter-channel isolation. It studies the impact of the different components of the scanning time, such as switching, communication, acquisition times, and the system dynamics on imaging performance and monitoring capabilities, optimizing the system setting while identifying system bottlenecks. The system uses an upgraded antenna-matching module and is experimentally validated using a mimicked hemorrhagic stroke-evolving scenario, demonstrating the effectiveness of both switching solutions in tracking and localizing the stroke progression. Tests of repeatability and sensitivity to false positive cases are also reported.**

***Index Terms*—Biomedical electromagnetic imaging, brain stroke, microwave antennas, microwave imaging.**

I. Introduction

A *stroke* is a severe life-threatening emergency caused by disrupted blood flow due to an artery rupture, vessel leak, or blood clot [1]. This condition induces changes in the dielectric properties of the affected tissues, with an increase of their value in the case of bleeding (hemorrhage, HEM) and a decrease during ischemia (IS) [2]. Such changes create a dielectric contrast with respect to the healthy scenario that can be detected by a microwave imaging (MWI) system, allowing to perform the diagnosis (detection and classification of the stroke), and follow-up of the disease after its onset. Despite their limitation in terms of spatial resolution (in the order of centimeters, which is anyway suitable for the relevant clinical conditions), MWI solutions complement the medical imaging panorama, providing a non-ionizing, portable, and cost-effective alternative with the potential for pre-hospital diagnosis, bedside imaging, and post-acute monitoring [3], [4], [5], [6], [7].

MWI retrieves contrast dielectric maps using back-scattered signals from the domain of interest (DoI), and proper inversion algorithms [8], [7], [9]. A typical MWI device comprises a transceiver system, e.g., a Vector Network Analyzer (VNA), multiple antennas, and a processing unit rendering the imaging [4]. Moreover, some configurations use a switching matrix (Sw-M) routing between an $n-$port transceiver and the $m-$antenna array. This approach is mainly convenient because it reduces the complexity and cost of the transceiver system, but adds a switching component that may affect the overall performance.

The Sw-M can be based on electromechanical or solid-state technologies. The electromechanical Sw-M relies on the physical movement of mechanical contacts, featuring low insertion loss, albeit switching time in the order of milliseconds, a large footprint, and a lifetime of about 10 million cycles. On the other hand, solid-state-based Sw-M switches employ electronic switches, typically either a PIN diode or cold FET circuit, or some combination thereof. These are prone to higher path attenuation compared to electromechanical counterparts and have switching time in the order of microseconds, superior resistance to shock and vibration, compact footprint, and long-lasting lifetime [10].

The selection of a suitable switching technology for an MWI system determines the performance of the imaging capabilities, as well as depends on problem-specific factors. For instance, in microwave imaging, the Sw-M is expected not to deteriorate the information content of the signals back-scattered by the inspected area, which the imaging algorithm requires to reproduce the studied scenario correctly. Moreover, time is also relevant in applications such as monitoring brain stroke. So, different systems for breast and brain imaging opted for both solid-state and electromechanical Sw-M [11], [12], [13], [14], [15], [16].

Manuscript received XXX, 2024; accepted XXX. Date of publication XXX; date of current version XXX. This work was supported in part by the project PON Research and Innovation "Microwave Imaging and Detection powered by Artificial Intelligence for Medical and Industrial Applications (DM 1062/21)", funded by MUR, by the Agritech National Research Center, funded by the Next-Generation EU (PNRR – MISSIONE 4 COMPONENTE 2, INVESTIMENTO 1.4 – D.D. 1032 17/06/2022, CN00000022), by the research project "MedWaveImage", funded by Interreg Central Europe (CE0200670) and by the research project "3BAtwin" funded by Horizon EU FP (101159623). *(Corresponding author: Francesca Vipiana)*

M. Gugliermino, D. O. Rodriguez-Duarte, C. Origlia, J. A. Tobon Vasquez and F. Vipiana are with the Department of Electronics and Telecommunications, Politecnico di Torino, 10129 Torino, Italy (e-mail: francesca.vipiana@polito.it).

R. Scapaticci and L. Crocco are with the Institute for the Electromagnetic Sensing of the Environment, National Research Council of Italy, 80124 Naples, Italy (e-mail: scapaticci.r@irea.cnr.it; crocco.l@irea.cnr.it).

J. Ch. Bolomey is with Universitè Paris-Saclay, Paris, France and eV-Technologies, Caen, France (e-mail: jcbelex@orange.fr).

Color versions of one or more of the figures in this letter are available online at http://ieeexplore.ieee.org.

Digital Object Identifier XXXXXXXXXXXXXXXX

This article has been accepted for publication in IEEE Antennas and Wireless Propagation Letters. This is the author's version which has not been fully edited and content may change prior to final publication. Citation information: DOI 10.1109/LAWP.2024.3435341

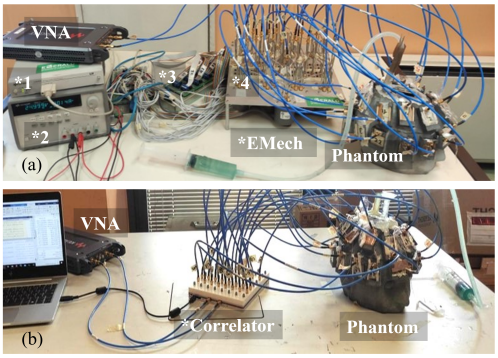

Fig. 1. Experimental setup using the pMWI system-based EMech and Correlator Sw-M in (a) and (b), respectively. The (*) indicates all the elements of the corresponding Sw-M.

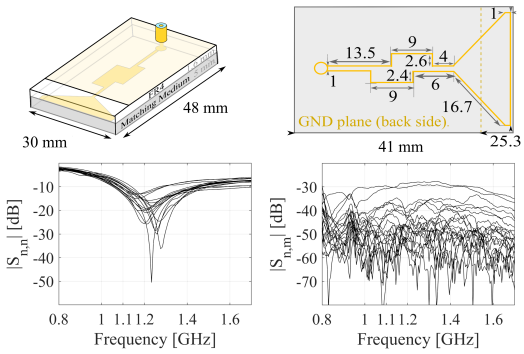

Fig. 2. Top: antenna scheme. Bottom: measure the reflection and transmission coefficients' amplitude using the Correlator.

This study concentrates on an upgraded multiview portable MWI (pMWI) scanner designed for stroke monitoring, whose previous versions have proven capable of experimentally monitoring the evolution of HEM and IS strokes within realistically mimicked environments [9], [14]. Specifically, the new system uses optimized antenna-matching modules and tests electromechanical and solid-state Sw-M, denoted in the following as EMech and Correlator, respectively. The two Sw-M connect a 2-port VNA to an array with twenty-two Antenna-Matching Module (Ant-MM). The analysis presented in this paper consists of two parts. The first part analyzes the scanning time and the trade-off with the MWI system dynamic, hence going beyond a technology comparison and delving into their limiting effects on an actual device operation. The second part focuses on the imaging capabilities of the MWI systems exploiting EMech or Correlator, respectively, in an experiment mimicking an evolving HEM condition.

II. Portable Microwave Imaging System

The pMWI system comprises a laptop, HP EliteBook 830 G5 with 8 GB RAM, a compact P5003B VNA [17], a Sw-M, EMech or Correlator, and twenty-two antennas placed around the head phantom, which is an anthropomorphic thin plastic container filled with a liquid mimicking the average dielectric properties of brain tissue. The system is shown in Fig. 1. The laptop is devoted to the setting and control of the measurement system, as well as to the processing of the measured data. The image formation is performed in real-time, taking just a couple of seconds, using a differential linear inversion algorithm based on the distorted Born approximation and a truncated singular value decomposition (TSVD) scheme, coupled with an artifact removal strategy [9]. As far as the scope of this article is concerned, the antennas and the Sw-M are further described in the following.

A. Antenna-Matching Module

Based on the design presented in [9], we optimize the Ant-MM, reducing the complexity of manufacturing by joining a printed monopole in a FR4 substrate and a slab of the matching medium as depicted in the top row of Fig.2. The matching medium is made of a mixture of 30% graphite powder and 70% urethane rubber, presenting a complex permittivity of $\epsilon_r = 20$ and $\sigma = 0.16$ S/m at 1.1 GHz. Moreover, thanks to the antenna's flexibility and softness, the antenna array can easily conform to the head shape, minimizing the air gap between the head and the antenna.

The optimized Ant-MM is designed to work in direct contact with the head surface, operating around 1.1 GHz in accordance with and supported by the rigorous design guidelines detailed in [18], [19]. This frequency choice is intended to reach a balance between the electromagnetic (EM) field penetration depth into brain tissues and the achievable spatial resolution, which is expected to be in the order of 5 mm [20]. Transmission parameter pairs fall between -80 and -30 dB, and the reflection parameters resonate around 1.2 GHz, as shown in the bottom of Fig.2. The latter's variability is due to positioning and manufacturing issues.

B. Switching Matrices

EMech is an ad-hoc matrix comprised of two single-pole four-throw (SP4T), eight single-pole-six-throw (SP6T), and twenty-four single-pole-double-throw (SPDT) electromechanical coaxial switches [21], [22], creating a 2×24 configuration, as detailed in [9]. The SP4T switches are connected to the VNA ports using flexible coaxial cables, while the SPDT switches are connected to each antenna using the same kind of cables. Connections between switches are made via rigid coaxial cables with uniform path lengths. In the whole considered frequency bandwidth, 0.8 – 1.8 GHz, EMech shows a single path attenuation less than 0.9 dB, a matching lower than -20 dB, and a channel isolation exceeding 90 dB [22]. Timing aspects of both matrices are explored in Sect. III-A.

It is worth noticing that in addition to the switches themselves (component *4 in Fig. 1(a)) , this setup also requires an external power supply, a communication board, and the control module, component *1,*2,*3, respectively, in Fig. 1(a), making the whole Sw-M bulkier. The dimension of the EMech Sw-M is about $30 \times 80 \times 20\,\text{cm}^3$.

The Correlator is an off-the-shelf solid-state Sw-M [23] that achieves a single path attenuation less than 4.9 dB, a matching below -15 dB up to 1.4 GHz and below -10 dB up to 1.8 GHz, and a measured isolation level exceeding 80 dB. It is a compact unit that does not require an external supply

This article has been accepted for publication in IEEE Antennas and Wireless Propagation Letters. This is the author's version which has not been fully edited and content may change prior to final publication. Citation information: DOI 10.1109/LAWP.2024.3435341

or a communication board. For this test, we employ a 2×64 version, which is the one available in our lab, though only 22 output ports are used. As illustrated in Fig. 1(b), the Correlator is clearly more portable than the EMech system, having a dimension of $15 \times 18 \times 2.5\,\mathrm{cm}^3$.

C. Calibration Procedure

To calibrate the system, we assume the same electrical paths between the ports of the antenna and the VNA. In the EMech case, we guarantee the same electrical length for all paths since all paths are designed and manufactured with the same physical length. As for the Correlator, we first measured the electrical path from the VNA ports to all available 64-antenna ports, and then we selected 22 paths with the same electrical length. Next, we implement a full-port calibration to either Sw-M in a systematic two-step process: (I) 2-port calibration and (II) calibration extrapolation. (I) We performed a 2-port calibration of one of the selected pair paths, using an E-Cal module [24]. Thus, we translate the calibration plane at the antenna ports. (II) The obtained calibration coefficients are then applied to all the other pairs before measuring the 22×22 scattering matrix. This calibration allows to obtain a maximum variation in magnitude within 0.2 dB and in phase within 0.1 deg respect to a standard full-port 22×22 calibration, which require at least $4n$ - 1 measurements, where n is the number of ports [25].

III. System Evaluation

In this section, the acquisition time with respect to the VNA intermediate filter (IF) is first assessed, and then the effect of the switching on the system's monitoring capabilities is investigated, presenting an analysis of the overall trade-off between measurement time, system dynamics and imaging performance. For the measurements, we use MATLAB v2023b to control the VNA and the EMech via VISA standard over TCP/IP I/O interfaces, using USB and Ethernet connections, respectively. Moreover, the Correlator is controlled by a serial port connection, running over USB, using the serial-port function of the Instrument Control Toolbox. To read the scattering data, we employ the MATLAB readbinblock function, which is set up with double precision and transfers the data via the VISA–TCP/IP connection.

A. Measurement Time Analysis

Let $T_{\mathrm{scan}} = T_{\mathrm{sw}}^{M} + T_{\mathrm{meas}}$, be the time required for a complete patient scan, i.e., the time required to acquire the whole $N_a^2 \times N_f$ scattering matrix, where N_a is the number of antennas and N_f is the number of frequency points, and T_{sw}^{M} standing for the total switching time, with M indicating EMech or Correlator, and T_{meas} for the measuring time.

In turn, T_{sw}^{M} depends on the kind of switching matrix, the single switch time, t_{sw}, and the communication time between the control unit and the switching matrix, t_{com}, as:

$$T_{\mathrm{sw}}^{M} = (t_{\mathrm{sw}} + t_{\mathrm{com}}) \cdot N_{\mathrm{sw}}, \tag{1}$$

where N_{sw} is the total number of switch steps required to form the whole scattering matrix and is given by $((N_a - 1)/2)N_a$.

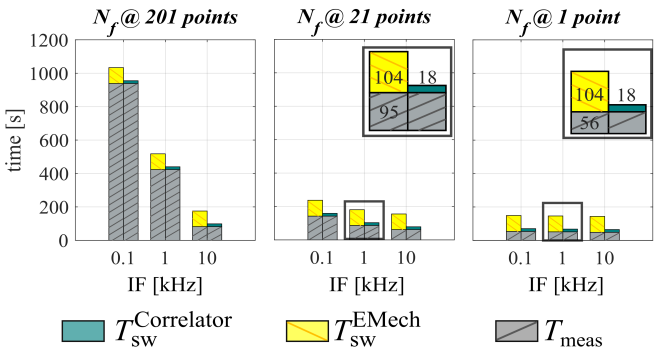

Fig. 3. Time analysis for gathering a 22×22 scattering matrix.

On the other hand, T_{meas} is dictated by the specifications and settings of the VNA, encapsulated in the acquisition time, t_{VNA}, as well as by the data saving time, t_{save}, which indicates the time required to transfer and save the $2 \times 2 \times N_f$ scattering matrix from the VNA to the imaging processing unit, i.e., the laptop. Notably, because the full $22 \times 22 \times N_f$ is filled sequentially, we have:

$$T_{\mathrm{meas}} = (t_{\mathrm{VNA}} + t_{\mathrm{save}}) \cdot N_{\mathrm{sw}}. \tag{2}$$

Figure 3 reports a graph indicating the required measurement time for different IF and N_f, showing, as expected, an overall decrease of measurement time with higher IF and an increment with N_f. Then, it can be noticed that T_{meas} scales down linearly with N_f respect to each IF, but when N_f tends to 1, the selection of the IF is less influential because T_{meas} is dominated by t_{save}. Moreover, T_{sw}^{M} remains constant for both EMech and Correlator for all configurations, having a $5\times$ gain for the Correlator (see values in Fig. 3). In the case of $N_f = 201$, T_{scan} is always dominated by T_{meas}. In cases that required small N_a, it is observed that for the EMech case, T_{meas} and T_{sw}^{M} are comparable across all three configurations (each nearly 50%), whereas in the Correlator case, T_{meas} is the dominant term. It is worth noting that t_{com} and t_{save} become a bottleneck for fast-measuring setups. For instance, even if solid-state-based switching technologies work with speeds in the order of μs, this can be degraded to ms due to communication issues.

B. IF Filter Analysis

This section is concerned with the selection of the optimal IF as a trade-off between measurement time and imaging performance. In the differential imaging scheme herein adopted, the input of the inversion algorithm is the differential scattering matrix obtained from the difference of the matrices measured at two different time-instants during the follow-up. Since at each instant the device measures the scattering matrix due to the whole head, sufficiently accurate measurements must be carried to faithfully extract the "useful" signal from the measured one. The available VNA shows a measured dynamic range (DR) of 130, 120, and 110 dB with an IF of 0.1, 1, and 10 kHz, respectively [17]. In the analysis performed to design the first device prototype [19], these DR values allow to

This article has been accepted for publication in IEEE Antennas and Wireless Propagation Letters. This is the author's version which has not been fully edited and content may change prior to final publication. Citation information: DOI 10.1109/LAWP.2024.3435341

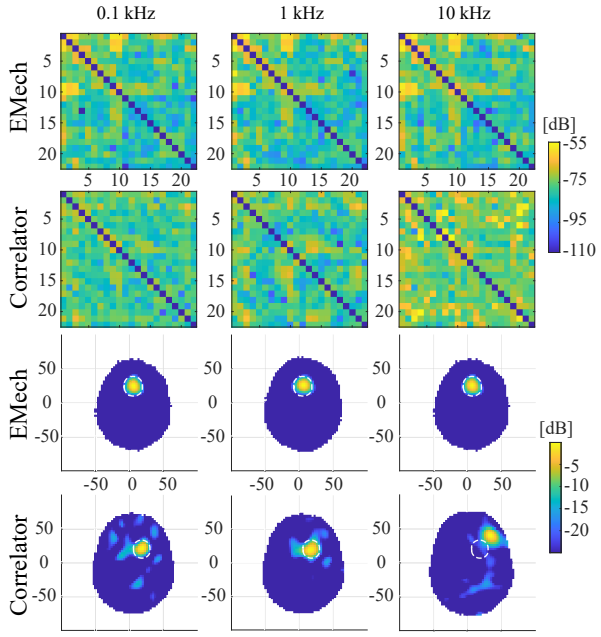

Fig. 4. Two detection experiments using EMech and Correlator-based systems. Top: differential scattering matrices. Bottom: normalized dielectric contrast sliced in the middle of the stroke region. The dotted contours indicate the expected position and shape of the stroke variation.

appraise a differential scattering matrices corresponding to volume variations in the order of $30\,\mathrm{cm}^3$, while the noise level is consistently low. Accordingly, the selection of the appropriate IF can be performed considering the noise introduced by the SW-M in the measurement process. To investigate this effect, we have designed a slightly more challenging (and realistic) experiment in which there is a $20\,\mathrm{cm}^3$ volume increase due to the insurgence of a HEM stroke from a healthy condition. We have performed the measurements with both the Sw-M, repeating them three times, for the different IF values. Fig.4 shows the differential scattering matrices measured at 1.1 GHz with their corresponding imaging results. As can be noticed, the imaging performance is comparable for all considered IFs. However, with the Correlator at 10 kHz, the S-parameters are corrupted, provoking a wrong localization, mainly due to its higher path attenuation, which becomes critical when less accurate measurements are performed. Therefore, monitoring measurements are conducted using a 1 kHz IF, which allows for accurate reconstruction, while reducing the measurement time as compared to 0.1 kHz IF. Finally, it is worth noting that as long as T_{scan} is dominated by T_{meas}, the imaging results can be improved for instance using a multi-frequency imaging algorithm processing up to $N_f = 21$ frequencies.

C. False Positive

To verify the robustness of the device to false positive cases, the data collected from the same scenario (healthy condition) at different times is used as input for the imaging algorithm. The findings are reported in Fig. 5 and show that the differential scattering matrices achieve lower values (below

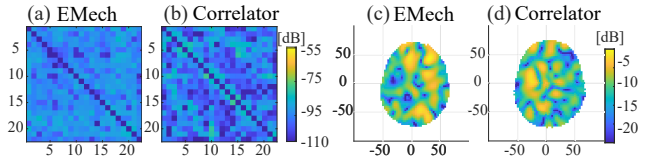

Fig. 5. False positive test. (a-b): the differential scattering matrices. (c-d): normalized dielectric contrast sliced at the maximum.

$-90\,\mathrm{dB}$), and the corresponding imaging results do not focus on any target.

D. Stroke Monitoring

As a final assessment, two different experiments are used to evaluate the monitoring capabilities achieved with both Sw-M. These replicate the procedure in [9], consisting of a HEM scenario evolving from 0 to $40\,\mathrm{cm}^3$, emulated with a balloon filled with an alcohol-based liquid with the dielectric properties of blood. Figure 6 depicts the monitoring results, representing volume variations of the stroke of $0 - 20\,\mathrm{cm}^3$ and $20 - 40\,\mathrm{cm}^3$, respectively. For EMech and Correlator, the sagittal views of normalized contrast are centered at their respective maximum. Observing the image, one can infer that the shape using values above $-3\,\mathrm{dB}$, indicated by the yellow zone. Note that two different experiments have been performed, one for each Sw-M configuration, so that the position of the target and its actual evolution is different between the two cases.

IV. Conclusion

This work studied the effects of the switching technology on the operation performance of a multi-view and low-complexity pMWI system for brain stroke monitoring. First, a time analysis identified that, in addition to the switching and the data acquisition times, (essential parameters for a real-time operation) that depend on the switching technology and the system dynamic, it is also critical to consider communication and data saving times since these became the operation bottleneck. Second, it was verified that the imaging monitoring capabilities were comparable regardless of the switching technology, though, this was degraded for the Correlator solution when a higher VNA IF was set. However, the Correlator allowed a significant reduction in the device's dimensions, representing an essential advancement towards the deployment in pre-hospital and bedside conditions.

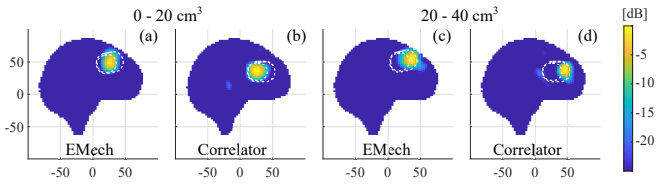

Fig. 6. Monitoring of stroke progression – comparison of the imaging results between the two configurations. Sagittal view of the normalized reconstructed dielectric contrast across the middle of the stroke. (a-b) present the progression from healthy state to a $20\,\mathrm{cm}^3$ stroke, and (c-d) the progression from a $20\,\mathrm{cm}^3$ stroke to a $40\,\mathrm{cm}^3$ stroke.

V. Acknowledgments

We thank eV-Technologies for providing us with the Correlator and technical support. We thank Eng. Simone Corallo and Eng. Silvia Garino for supporting the measuring campaign.

References

[1] C. W. Tsao, A. W. Aday, Z. I. Almarzooq, C. A. Anderson, P. Arora, C. L. Avery, C. M. Baker-Smith, A. Z. Beaton, A. K. Boehme, A. E. Buxton *et al.*, "Heart disease and stroke statistics—2023 update: a report from the american heart association," *Circulation*, vol. 147, no. 8, pp. e93–e621, 2023.

[2] B. Norrving, "Classification of stroke subtypes,," in *Stroke. Practical guide for clinicians*. Karger: Basel, 2009.

[3] A. Fhager, S. Candefjord, M. Elam, and M. Persson, "Microwave diagnostics ahead: Saving time and the lives of trauma and stroke patients," *IEEE Microwave Magazine*, vol. 19, no. 3, pp. 78–90, 2018.

[4] L. Guo, A. S. Alqadami, and A. Abbosh, "Stroke diagnosis using microwave techniques: Review of systems and algorithms," *IEEE Journal of Electromagnetics, RF and Microwaves in Medicine and Biology*, vol. 7, no. 2, pp. 122–135, 2022.

[5] D. Cook *et al.*, "Case report: Preliminary images from an electromagnetic portable brain scanner for diagnosis and monitoring of acute stroke," *Front Neurol*, vol. 12, p. 765412, oct 2021.

[6] A. Abbosh *et al.*, "Clinical electromagnetic brain scanner," *Scientific Reports*, vol. 14, no. 1, p. 5760, Mar 2024. [Online]. Available: https://doi.org/10.1038/s41598-024-55360-7

[7] A. Fedeli, V. Schenone, A. Randazzo, M. Pastorino, T. Henriksson, and S. Semenov, "Nonlinear s-parameters inversion for stroke imaging," *IEEE Transactions on Microwave Theory and Techniques*, vol. 69, no. 3, pp. 1760–1771, 2021.

[8] D. Cook, H. Brown, I. Widanapathirana, D. Shah, J. Walsham, A. Trakic, G. Zhu, A. Zamani, L. Guo, A. Brankovic *et al.*, "Case report: Preliminary images from an electromagnetic portable brain scanner for diagnosis and monitoring of acute stroke," *Frontiers in neurology*, vol. 12, p. 765412, 2021.

[9] D. O. Rodriguez-Duarte, C. Origlia, J. A. T. Vasquez, R. Scapaticci, L. Crocco, and F. Vipiana, "Experimental assessment of real-time brain stroke monitoring via a microwave imaging scanner," *IEEE Open Journal of Antennas and Propagation*, vol. 3, pp. 824–835, 2022.

[10] M. Sayed and J. Martens, *Vector network analyzers*, ser. The Cambridge RF and Microwave Engineering Series. Cambridge University Press, 2013, p. 98–129.

[11] O. Zaatar, A. Zakaria, and N. Qaddoumi, "A novel switch for microwave imaging systems," *IEEE Access*, vol. 12, pp. 26 978–26 990, 2024.

[12] Y. Akazzim, M. Jofre, O. El Mrabet, J. Romeu, and L. Jofre-Roca, "Uwb-modulated microwave imaging for human brain functional monitoring," *Sensors*, vol. 23, no. 9, p. 4374, 2023.

[13] N. Valizade Shahmirzadi, N. K. Nikolova, and C.-H. Chen, "Interconnect for dense electronically scanned antenna array using high-speed vertical connector," *Sensors*, vol. 23, no. 20, 2023. [Online]. Available: https://www.mdpi.com/1424-8220/23/20/8596

[14] J. A. Tobon Vasquez, R. Scapaticci, G. Turvani, G. Bellizzi, D. O. Rodriguez-Duarte, N. Joachimowicz, B. Duchêne, E. Tedeschi, M. R. Casu, L. Crocco *et al.*, "A prototype microwave system for 3d brain stroke imaging," *Sensors*, vol. 20, no. 9, p. 2607, 2020.

[15] S. Semenov, R. Planas, M. Hopfer, A. Hamidipour, A. Vasilenko, E. Stoegmann, and E. Auff, "Electromagnetic tomography for brain imaging: Initial assessment for stroke detection," in *2015 IEEE Biomedical Circuits and Systems Conference (BioCAS)*, 2015, pp. 1–4.

[16] Q. Mahmood, S. Li, A. Fhager, S. Candefjord, A. Chodorowski, A. Mehnert, M. Persson *et al.*, "A comparative study of automated segmentation methods for use in a microwave tomography system for imaging intracerebral hemorrhage in stroke patients," *Journal of Electromagnetic Analysis and Applications*, vol. 7, no. 05, p. 152, 2015.

[17] "Streamline series vector network analyzer," Available at https://www.keysight.com/us/en/products/network-analyzers/streamline-series-usb-vector-network-analyzers/p50xxb-streamline-series-vector-network-analyzers.html.

[18] R. Scapaticci, L. Di Donato, I. Catapano, and L. Crocco, "A feasibility study on microwave imaging for brain stroke monitoring," *Progress In Electromagnetics Research B*, vol. 40, pp. 305–324, 2012.

[19] R. Scapaticci, J. Tobon, G. Bellizzi, F. Vipiana, and L. Crocco, "Design and numerical characterization of a low-complexity microwave device for brain stroke monitoring," *IEEE Transactions on Antennas and Propagation*, vol. 66, no. 12, pp. 7328–7338, 2018.

[20] D. O. Rodriguez-Duarte, J. A. T. Vasquez, R. Scapaticci, L. Crocco, and F. Vipiana, "Assessing a microwave imaging system for brain stroke monitoring via high fidelity numerical modelling," *IEEE Journal of Electromagnetics, RF and Microwaves in Medicine and Biology*, vol. 5, no. 3, pp. 238–245, 2021.

[21] J. A. Tobon Vasquez, R. Scapaticci, G. Turvani, G. Bellizzi, N. Joachimowicz, B. Duchêne, E. Tedeschi, M. R. Casu, L. Crocco, and F. Vipiana, "Design and experimental assessment of a 2d microwave imaging system for brain stroke monitoring," *International Journal of Antennas and Propagation*, vol. 2019, pp. 1–12, 2019.

[22] "Keysight datasheet," Available at https://www.keysight.com/us/en/product/87204C/87204c-multiport-coaxial-switch-dc-to-26-5-ghz-sp4t.html.

[23] "Dual evt1016 datasheet," Available at https://ev-technologies.com/portfolio-items/dual-evt1016/.

[24] "Keysight datasheet," Available at https://www.keysight.com/us/en/product/N7551A/electronic-calibration-module-ecal-dc-6-5-ghz-2-port.html.

[25] M. S. Valeria Teppati, Andrea Ferrero, *Multiport S-parameters measurement methods*. Cambridge University Press, 2013, pp. 219–239.